Optics Communications 537 (2023) 129394

Contents lists available at ScienceDirect

Optics Communications

journal homepage: www.elsevier.com/locate/optcom

The evolution of hot spot and nanojet by engineering the local modes of microcylinder

Yi Xing [a,b], Yihui Wu [a,*], Yue Wang [a], Tianyu Zhao [a,b], Wenchao Zhou [a,*], Fengfeng Shu [a]

[a] Changchun Institute of Optics, Fine Mechanics and Physics, Chinese Academy of Science, Changchun 130033, China
[b] University of Chinese Academy of Sciences, Beijing 100039, China

ARTICLE INFO

Keywords:
Microcylinder
Hot spot
Micro-optics
Local modes

ABSTRACT

Hot spot and photonic nanojet (PNJ) are subwavelength focused beams generated from the microsphere or microcylinder. In this paper, we proposed a method of excitation of high-order resonant modes in microcylinder with a high-refractive index cladding and modulation of local modes at the exit end to generate the hot spot. A hot spot with a full width at half maximum waist of 66.70nm(λ/8.47) on the surface is obtained and explained by the wave superposition theory modulated by local modes. The influence of local structures and refractive index on the waist, effective length and exit direction of the hot spot is discussed. The focal position of the hot spot can be gradually moved out and converted to the nanojet by engineering the local modes of the microcylinder. Also, a cubic array chip is suggested for decreasing the difficulty of manufacture. And it shows that number and position of the hot spot can be controlled by adjusting the refractive index and height of the local structure. This work provides a possibility for potential applications in the fields of high-throughput super-resolution near-field imaging, localized excitation and imaging of single-molecule fluorescence.

1. Introduction

The ability of mesoscale dielectric particles (microspheres or microcylinders) to localize the optical wave below sub-wavelength volumes has attracted tremendous attentions in recent years. Photonic nanojet is a high-intensity narrow focus beam which can be generated from microparticles illuminated with a plane wave. PNJ has the characteristics of high-intensity super-resolution focusing and easy assembly [1], which has broad applications in Microsphere-assisted Microscopy [2–5], Fluorescence Sensing [6,7], Photolithography [8]. The mechanism of PNJ's formation, the characteristic of microspheres with different structures and their key parameters (such as full width at half maximum (FWHM), peak intensity, effective length (L)) have already been extensively discussed in resonant or non-resonant conditions [9–19]. And optical phenomena in Janus particles also attracts great attentions [20–22].

In addition, hot-spot engineering also has the ability to localize optical waves to sub-wavelength scale, and the waist is below the diffraction limit. Hot spots of metal nanoparticles are created by the optical resonant excitation of localized surface plasmons. Due to the characteristics of great enhancement of electromagnetic field intensity, it is widely used in the field of surface-enhanced Raman spectroscopy (SERS) [23]. In order to obtain high-resolution and single-molecule-level detection, some research has used nanojet to excite hot spots of SERS metal nanoparticles [24,25]. Recent reports indicate that dielectric mesoscale particles can generate hot spots with the size of approximately λ/5 [26–28]. Hot spots in super-enhancement focusing [29] and magnetic field intensity enhancement [21] has been discussed. However, the focus of hot spots is localized inside the particles, relevant applications (super-resolution imaging or single-molecule detection) cannot directly utilize its best optical performance part. And the construction of hot spots which is beyond the diffraction limit and manufacturing-friendly is still under discussion.

In this paper, we propose a method to generate the hot spot by utilizing a high-refractive index cladding and modulating local modes at the exit end of the microcylinder. The hot spot with FWHM of 66.70 nm (λ/8.47) on the surface is achieved. The focal position of the hot spot can be adjusted and even be extended outward gradually by modulating the height of the local structures. Within a certain range, FWHM changes regularly with local structures. Field localization can be shifted from hot spot to nanojet by changing the refractive index and structural parameters. Based on this method, we introduce a cubic array chip to decrease difficulty of fabrication. Also, we can manipulate parameters of the local structure to control the number and position of the hot spot.

* Corresponding authors.
E-mail addresses: yihuiwu@ciomp.ac.cn (Y. Wu), zhouvc@ciomp.ac.cn (W. Zhou).

https://doi.org/10.1016/j.optcom.2023.129394
Received 20 October 2022; Received in revised form 18 February 2023; Accepted 24 February 2023
Available online 28 February 2023

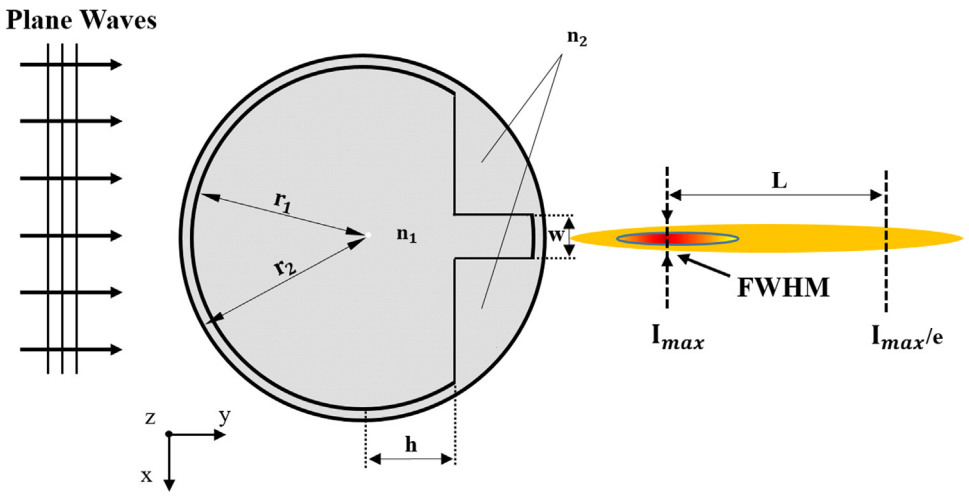

Fig. 1. Schematic of the model used in the numerical simulation.

2. Method and design

The simulation model is showed in Fig. 1, the transparent dielectric microcylinder is considered as a 2D structure extending infinitely along z-axis. Cartesian coordinate system is adopted here. The model is concentric with coordinates (0, 0). The microcylinder consists of an inner core of the refractive index n_1 with a radius r_1, a shell of the refractive index n_2 with a radius r_2 and two symmetrically embedded parts(local structures) of the refractive index n_2 with height h and distance w between each other. FWHM is the full width at half maximum of the focus. I_{max} is the peak intensity of the focal point. The effective length L is the distance from the point of I_{max} to the 1/e value point of I_{max}. We use the commercial finite element software COMSOL to calculate the electric field distribution of the model. The background is the air with the refractive index of 1. The illumination wave is a z-axis polarized plane wave propagating along y-axis. The maximum mesh size is 5 nm for model, 25 nm for background and the minimum mesh size is 0.4 nm for model to ensure accurate calculation. Perfect match layers are set for all boundaries.

3. Results and discussion

Generally, the localized beam formed by the high-refractive index microsphere can obtain a narrower waist or better imaging performance [30–32]. According to the higher index of refraction, the fraction of evanescent fields outside the Mie particles can be significantly increased [33]. The high-refractive index material is used as the cladding layer of the microcylinder to increase the mode order. The refractive index of the cladding is set as $n_2 = 3.5$ ($Al_xGa_{1-x}As$ [34], corresponding wavelength $\lambda = 565$ nm in vacuum). In this case, the internal refractive index must be set properly to form a narrow localized optical beam: if the difference between the internal and external refractive index is small, the transverse width of the focal point is wider [35]; while the refractive index contrast between the microcylinder and surrounding media is higher than 2, the localized optical beam will focus inside [36]. Thus, we select the normal glass with $n_1 = 1.43$. And the radius $r_1 = 6\lambda$, $r_2 = 6.2\lambda$. The embedded. parts spacing w is 0.2 um.

As depicted in Fig. 2(a), the embedded parts and the microcylinder generate WGM resonance together when h = 2.970 um. The resonance enhances the focal intensity and changes the local modes in embedded parts which makes the energy flow output in the set direction to form a narrow and intensity-enhanced localized optical beam (hot spot) when h = 2.983 um, as showed in Fig. 2(b). The FWHM of the surface of the structure is 66.70 nm ($\lambda/8.47$)(red curve in Fig. 2.(d)) which breaks the diffraction limit. Comparing inset 1 and 2 in Fig. 2; the spot size and energy of the local modes in embedded parts change with h. Comparing inset 3 and 4, it is found that except for the embedded parts, other parts of the microcylinder still keep original modes, but electric field intensity is weakened. And it is the change of the local modes in the embedded parts that causes the energy redistribution. The energy is coupled from the spot along the shell to the central hot spot, so that its intensity is enhanced to 58 times of the incident intensity. Under the resonance state, the transmission wave and the evanescent wave existing in the near region superimpose locally and generate fringes [37]. Destructive interference between fringes and hot spot results in energy redistribution, and then shrink the hot spot waist. Adjusting h is essentially to modulate the degree of wave superposition in local modes, which in turn affects destructive interference of fringes to the hot spot. Streamlines of Poynting vectors are showed in Fig. 2(c), the color bar represents the P_y value. The optical vortices can be clearly seen in the enlarged image. From the perspective of energy flow: energy exchange occurs at the optical singularity. Regulating h is also to adjust the block degree of optical singularity to main lobe. We simulate and plot the transverse intensity profiles of two structures in Fig. 2(d). The FWHM of a single dielectric microcylinder with n = 1.43 is 327 nm ($\lambda/1.73$). In comparison, the FWHM of our proposed structure is greatly reduced by 4.88 times.

The variations of FWHM and I_{max} of the hot spot at different positions along the y-axis from the surface are depicted in Fig. 3(a). It shows that the FWHM at 75 nm and 150 nm away from the surface is still less than 100 nm and 140 nm, respectively. Moreover, change the parameters w and h in 1 nm steps separately, the variations of FWHM and I_{max} are plotted in Fig. 3(b). The change range of h and w is about 20 nm. The star-label data represents the smallest FWHM. The local modes of the embedded parts and the main mode of the cylinder determine the minimum waist together. With the increase of h or w, the FWHM gradually increases, and the I_{max} first increases and then decreases. Because the destructive interference effect on the hot spot gradually weakens as h or w increases.

The variation curve of L with h is shown in the black curve in Fig. 3(c), and the overall trend of L increases as h increases. In order to express the optical characteristics of the hot spot and show the constraint relationship between waist, effective length and intensity, we introduce the quality criterion Q of nanojet: $Q = (I_{max} \times L)/FWHM$ [38], as shown in the blue curve in Fig. 3(c). The variation trend of Q with h is similar to that of I_{max}, both of which achieve the maximum value at h = 2.983 um. This indicates that there is the best compromise relationship between FWHM, L and Imax under this structural parameter. Fig. 3(d) is the change curve of the focus position of the hot spot. Dashed lines are structure boundary. We can find that as h increases, the focus position of the hot spot is gradually moving outward. This reveals that one can change the local structure

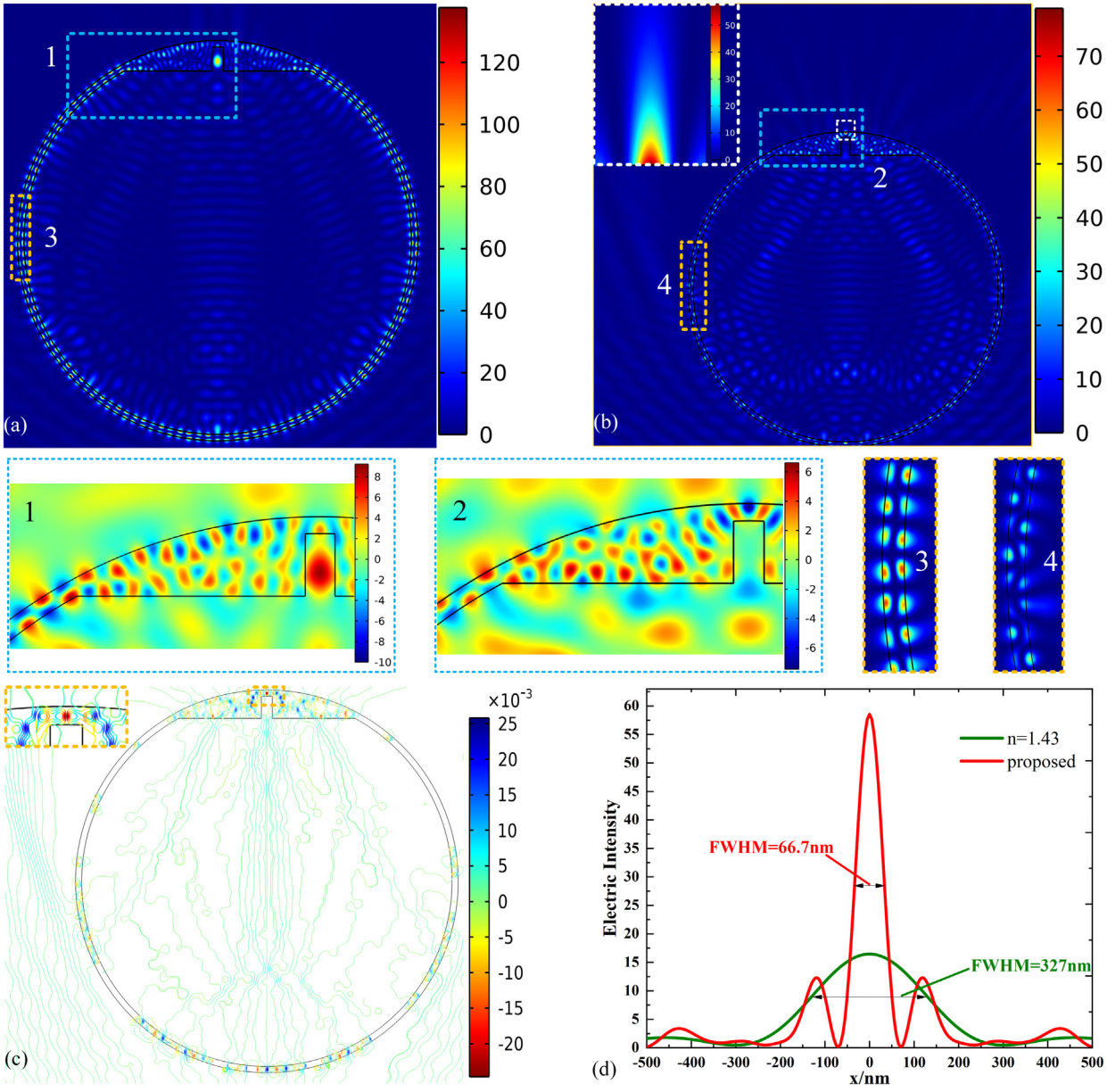

Fig. 2. (a) The electric field distribution of WGM resonance with h = 2.970 um. (b) The Electric field distribution with h = 2.983 um. The external hot spot is showed in enlarge image. Inset 1 and 2 are Ez distribution of (a) and (b). Inset 3 and 4 are enlarged view of electric field distribution of corresponding number. (c) Streamlines of Poynting vectors of (b). (d) The transverse intensity profiles of different structures.

parameters so that the hot spot is not fully localized in the interior, but gradually moves outward.

We plot the changing process of electric field distribution of hot spot with the focal gradually moving outward in Fig. 4(a)–(d). From these four images, it can be seen that the focus of hot spot is gradually moving outward with the increase of h. Modulating the height of the local structures will affect the wave superposition at the hot spot, which will cause the focus of the hot spot to move outward. In the supplementary material, video 1 and video 2 respectively show the change of whole electric field distribution, local electric field distribution and focal position of hot spot in more detail as h gradually increases. We found that as h increases, the focus position moves outward and the length of the hot spot also becomes longer. The gradually outward movement of the hot spot is beneficial for applications such as super-resolution imaging and single-molecule detection, so that we can take advantage of the good optical characteristics closer to the focus. In addition, we also found that changing local structural parameters, such as h and refractive index n_2, the hot spot can be transformed into nanojet, as depicted in Fig. 5. When $n_2 = 2.7$, $h = 5.40\lambda$, the nanojet can be obtained. The focus point is exactly at the border, and the electric field distribution is showed in Fig. 5(a); when $n_2 = 3.0$, $h = 5.96\lambda$, the classic nanojet is generated and its electric field distribution is showed in Fig. 5(b).

Next, we plot the scatter diagrams of the FWHM and effective length L of the hot spot changed with h when $n_2 = 3.5$(red), $n_2 = 3.405$ [34] (blue, corresponding wavelength is 654 nm in vacuum), $n_2 = 3.306$ [34] (green, corresponding wavelength is 654 nm in vacuum) in Fig. 6(a), and (b), respectively. By comparing three scatter plots in Fig. 6(a), the FWHM scatter plot with $n_2 = 3.5$ is generally lower than the other two, and it is obvious that the narrowest FWHM can be obtained when $n_2 = 3.5$. It demonstrates that the larger n_2 is, the narrower the FWHM can be obtained. Besides, the compression on lateral and longitudinal field distribution of hot spot are weakened with the decrease of n_2. As shown in Fig. 6(b), the smaller the n_2, the longer the L. The average value of the proportion of inside-hot-spot drops from 29.78% of $n_2 = 3.5$ to 23.91% of $n_2 = 3.405$, 19.34% of $n_2 = 3.306$. Thus the effective

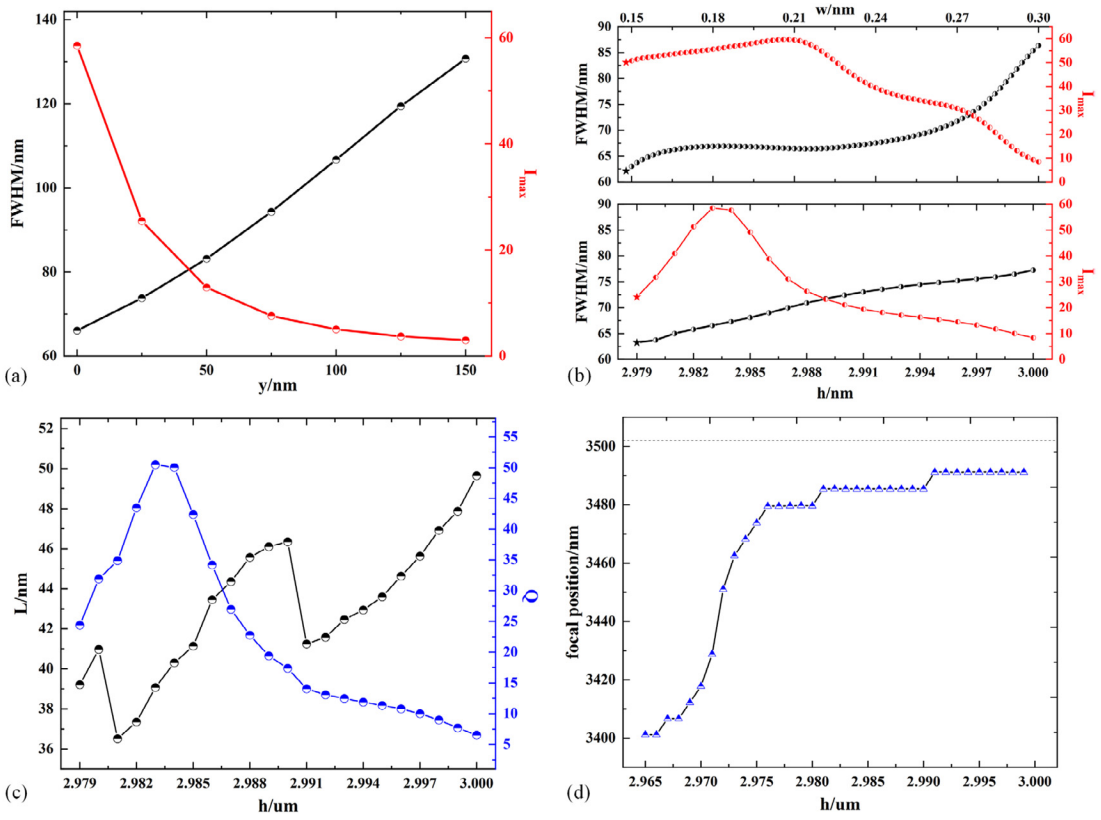

Fig. 3. (a) FWHM (black) and I_{max}(red) curves at different y from the surface. (b) Above and below are curves of FWHM and I_{max} varying with w and h, stars represent resonance. (c) The L (black) and quality criterion Q (blue) of the hot spot as a function of the h. (d) Focal position of the hot spot as a function of the h, dashed lines indicate structure boundary.

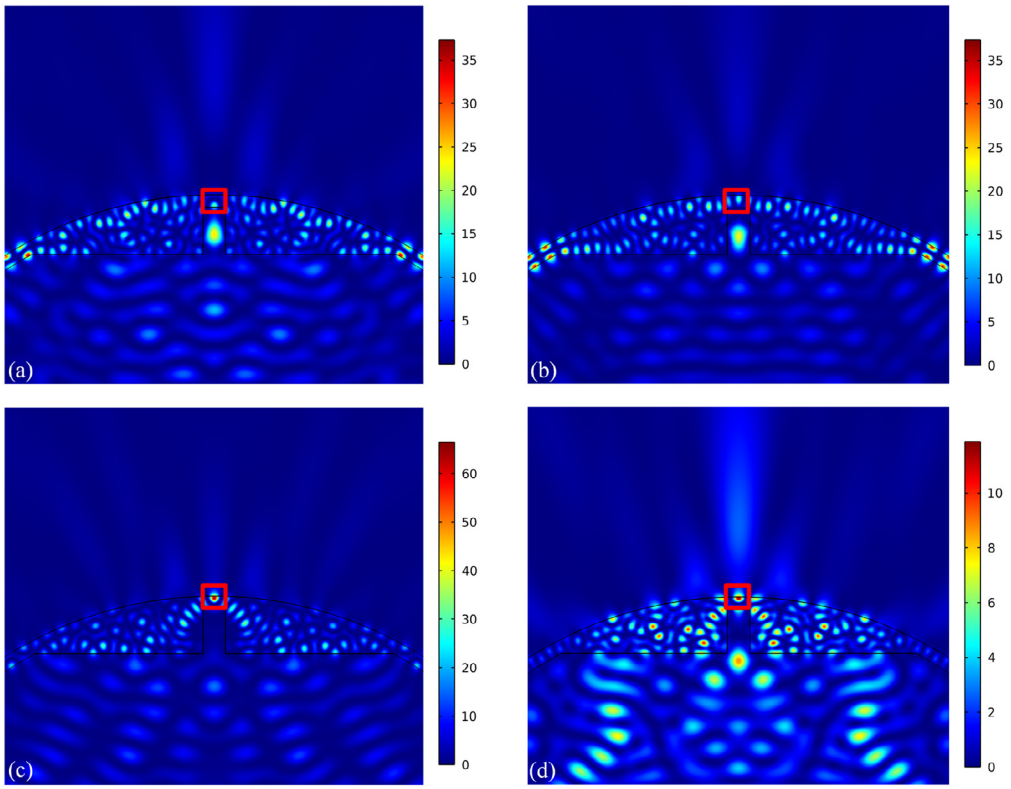

Fig. 4. The electric field distribution of the hot spot with different h. (a) h = 2.965 um. (b) h = 2.974 um. (c) h = 2.985 um. (d) h = 2.999 um. The red box marks the location of the hot spot.

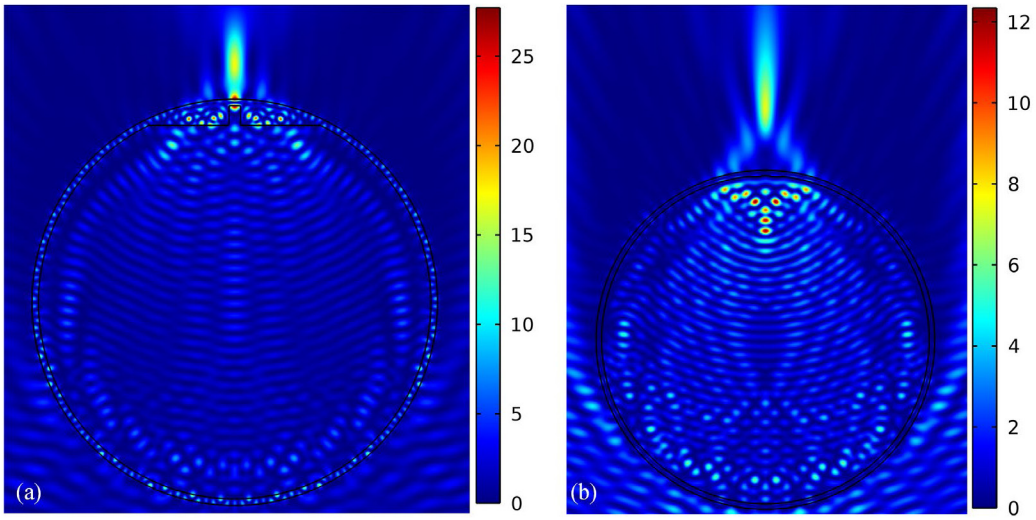

Fig. 5. The electric field distribution of the nanojet. (a) $n_2 = 2.7$, $h = 5.40\lambda$. (b) $n_2 = 3.0$, $h = 5.96\lambda$.

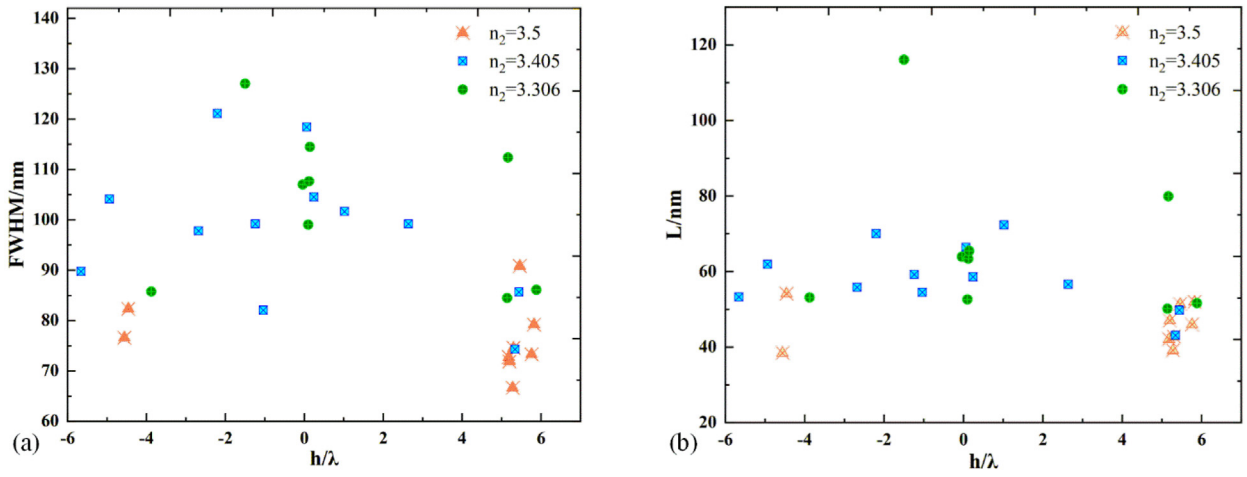

Fig. 6. (a) The scatter diagrams of FWHM with different n_2. (b) The scatter diagrams of effective length L with different n_2.

length can be increased by decreasing the n_2, so that the hot spot gradually extends outward at the expense of waist. There is always an objective trade-off between obtaining a narrower waist or a longer effective length. Fig. 7 shows the hot spot quality criterion as a function of the h and n_2. The Q has the maximum value when $n_2 = 3.5$, $h = 5.28\lambda$. In such parameter, the hot spot combines the advantage of narrow FWHM and high intensity.

If the n_2 increases gradually, the light tends to be transmitted close to the normal line because of the refraction angle becomes smaller. The hot spot in the middle part will be focused completely inside and the internal energy loss is extremely large due to the total internal reflection. Simulation shows that when n_2 is greater than 4.5, the modulation of h cannot form a centrally located hot spot in the near field of the structure, but can guide the energy flow to emerge from both sides to form a narrow multi beams. As shown in Fig. 8, the electric field distribution characteristics of the hot spot can be simply divided into two types after n_2 is greater than 4.5. The central hot spot is focused totally inside but form two hot spots from both sides in type-I, as illustrated in Fig. 8(a–c). While the central hot spot can still be generated in type-II in Fig. 8(d) with FWHM of 64.5 nm when n_2 is 4.5. It cannot converge at the center but will form two long localized beams from both sides in type-II in Fig. 8(e–f) after n_2 is greater than 4.5.

Besides, we popularize this method to the cubic array chip, as depicted in Fig. 9. The unit cell is made up of three materials: the

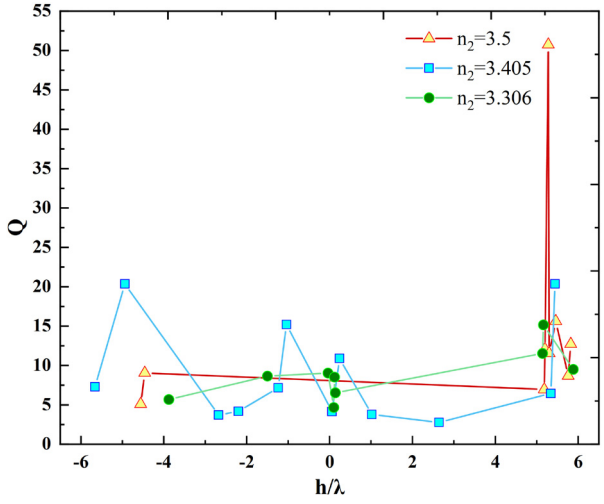

Fig. 7. The quality criterion Q of hot spot as a function of the h and n_2.

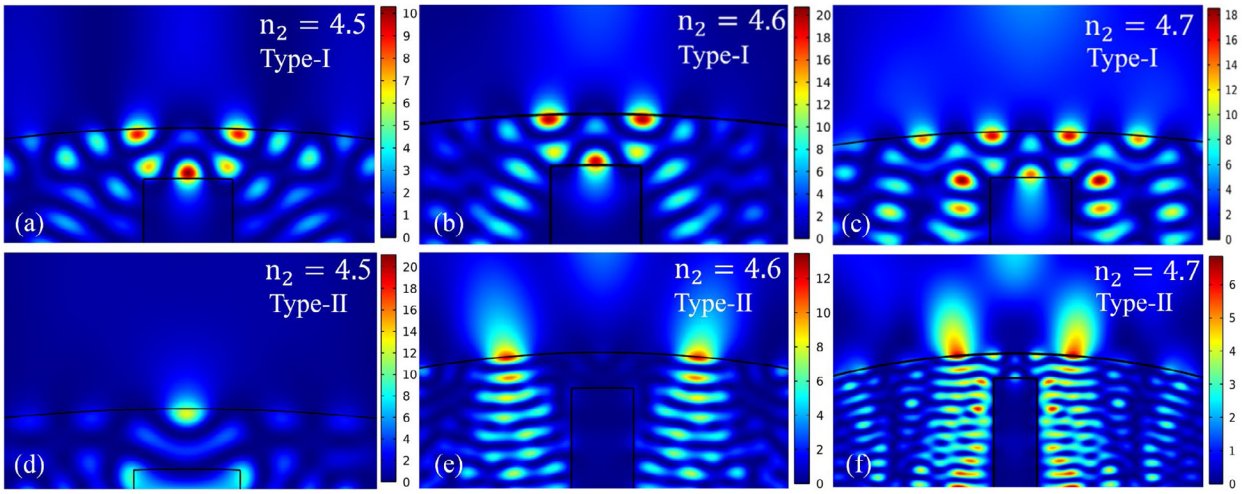

Fig. 8. Two types of electric field distribution after n_2 greater than 4.5. (a) h = −0.78 um, $n_2 = 4.5$. (b) h = 2.927 um, $n_2 = 4.6$. (c) h = 2.825 um, $n_2 = 4.7$. (d) h = 2.893 um, $n_2 = 4.5$. (e) h = 2.554 um, $n_2 = 4.6$. (f) h = 2.949 um, $n_2 = 4.7$.

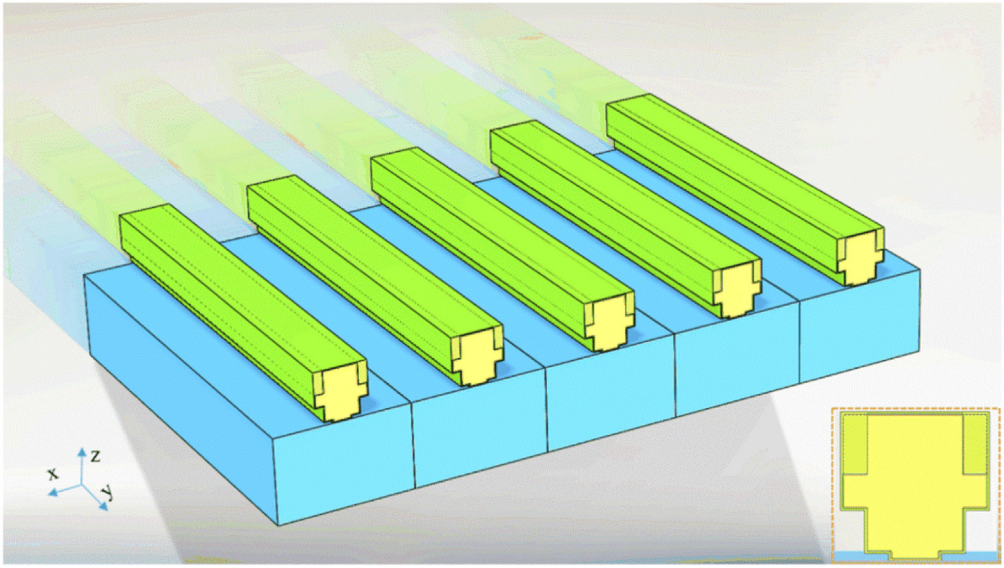

Fig. 9. Three dimensional diagram of cubic array chip, enlarged diagram is a unit cell.

shell (green) is TiO_2. The inner core (yellow) is glass [39], the width along x-axis is 1 um for both sides and 2 um for the middle part. The spacing between inner core and shell is 100 nm. The embedded height is h. A 50 um-thick SiO_2 is adopted as the substrate (blue). The left and right sides are replaced with periodic boundary conditions. The period is 16 um. The structure is illuminated perpendicularly along the positive z-axis. When h = 0.3 um, n = 1.53, two hot spots with FWHM of 108 nm are generated on both edge of surface, as shown in Fig. 10(a); when h = 1.5 um, n = 1.42, two hot spots with FWHM of 89 nm are generated on both sides of surface, as shown in Fig. 10(c); when h = 1.8 um, n = 1.40, three hot spots with FWHM around 120 nm can be obtained, as shown in Fig. 10(e). A zoomed-in view of the electric field distribution of the hot spot can be seen in Fig. 10(g–j). The streamlines of Poynting vectors is depicted in Fig. 10(b), (d), (f), respectively. Because the change in height of three cuboids at the bottom is used to fit the circular curvature, multiple directions of the energy flow are generated internally, and finally multi-beam are outputting under the guidance of the embedded parts. The number and position of the outgoing beams can be controlled by adjusting the embedded height h and the refractive index n. This method reduces the processing difficulties, and the addition of substrate and array is convenient for use. This structure can be fabricated by combination of two-photon laser direct writing technology and atomic layer deposition technology. Multi-beam is widely used in microfabrication and data storage [40,41].

4. Conclusion

In conclusion, we discuss the formation and evolution mechanism of the hot spot and nanojet by modulating of local modes of the engineered microcylinder. The effects of local structures and refractive index on the FWHM, effective length, hot spot exit direction and the modulation rule are given. Using $Al_xGa_{1-x}As$ with refractive index of 3.5, a narrow hot spot with high resonant mode and good internal optical transmission is constructed. The FWHM of 66.70 nm ($\lambda/8.47$) is realized through local modes regulation at the outlet. Without cutting the structure, FWHM is still less than 100 nm and 150 nm at 75 nm and 140 nm away from the surface, respectively. Numerical analysis shows: (1) When the volume and shell radius of the microcylinder are fixed, the overall highest resonant mode of the microcylinder depends on the refractive index of the inner core and the shell, the local modes of embedded parts and the main mode of the microcylinder together form

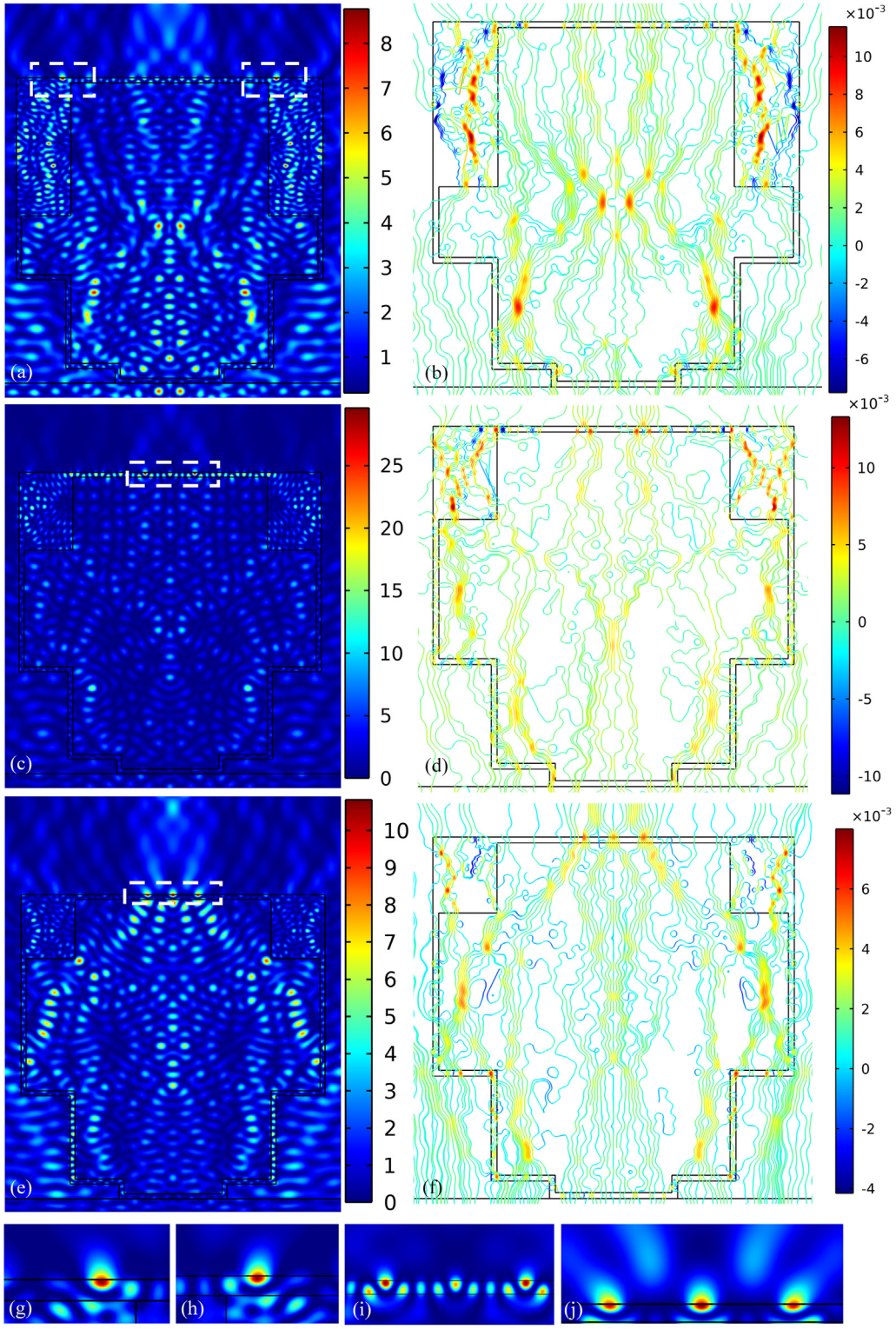

Fig. 10. (a), (c) and (e) are the electric field distribution when h = 0.3 um, n = 1.53, h = 1.5 um, n = 1.42 and h = 1.8 um, n = 1.40, respectively. (b), (d) and (f) are the streamlines of Poynting vectors of (a), (c) and (e), respectively. (g), (h) are the enlarged images of the dashed area on the left and right of (a), respectively. (i), (j) are the enlarged images of the dashed area of (c) and (e), respectively.

the minimum width of the hot spot; (2) Changing the embedded height h regulates destructive interference to shrink the waist. It is found that FWHM is positively correlated with the local structural parameters (h and w) within the change range of h and w of 20 nm. Reducing the refractive index n_2 and modulating h can make the hot spot gradually extend outwards and transform the hot spot to the nanojet. (3) Considering the manufacturing difficulty of spherical structure array, this work provides a design of cubic array chip with TiO_2 cladding. The implementation of this array provides a possibility for high-throughput super resolution near-field imaging, localized excitation and imaging

of single molecule fluorescence. The idea of modulating local modes in this work provides a new way for the design of microcylinder to localize optical wave in the future.

Declaration of competing interest

The authors declare the following financial interests/personal relationships which may be considered as potential competing interests: Yihuiwu reports financial support was provided by National Natural Science Foundation of China. Yihuiwu has patent pending to 202211560119.5.

Data availability

No data was used for the research described in the article.

Acknowledgments

This work was supported by the National Natural Science Foundation of China (U21A20395), and ShuGuang Talents Scheme Award of CIOMP, China.

Appendix A. Supplementary data

Supplementary material related to this article can be found online at https://doi.org/10.1016/j.optcom.2023.129394.

References

[1] X. Liang, R. Dong, J.C. Ho, Self-assembly of colloidal spheres toward fabrication of hierarchical and periodic nanostructures for technological applications, Adv. Mater. Technol. 4 (3) (2019) 1800541.
[2] Z. Wang, W. Guo, L. Li, B. Luk'Yanchuk, A. Khan, Z. Liu, M. Hong, Optical virtual imaging at 50 nm lateral resolution with a white-light nanoscope, Nature Commun. 2 (1) (2011) 1–6.
[3] X. Hao, X. Liu, C. Kuang, Y. Li, Y. Ku, H. Zhang, H. Li, L. Tong, Far-field super-resolution imaging using near-field illumination by micro-fiber, Appl. Phys. Lett. 102 (1) (2013) 013104.
[4] S. Lee, L. Li, Rapid super-resolution imaging of sub-surface nanostructures beyond diffraction limit by high refractive index microsphere optical nanoscopy, Opt. Commun. 334 (2015) 253–257.
[5] M. Duocastella, F. Tantussi, A. Haddadpour, R.P. Zaccaria, A. Jacassi, G. Veronis, A. Disapro, F.D. Angelis, Combination of scanning probe technology with photonic nanojets, Sci. Rep. 7 (1) (2017) 1–7.
[6] H. Aouani, F. Deiss, J. Wenger, P. Ferrand, N. Sojic, H. Rigneault, Optical-fiber-microsphere for remote fluorescence correlation spectroscopy, Opt. Express 17 (21) (2009) 19085–19092.
[7] H. Aouani, P. Schön, S. Brasselet, H. Rigneault, J. Wenger, Two-photon fluorescence correlation spectroscopy with high count rates and low background using dielectric microspheres, Biomed. Opt. Express 1 (4) (2010) 1075–1083.
[8] W. Wu, A. Katsnelson, O.G. Memis, H. Mohseni, A deep sub-wavelength process for the formation of highly uniform arrays of nanoholes and nanopillars, Nanotechnology 18 (48) (2007) 485302.
[9] D.S. Benincasa, P.W. Barber, J.Z. Zhang, W.F. Hsieh, R.K. Chang, Spatial distribution of the internal and near-field intensities of large cylindrical and spherical scatterers, Appl. Opt. 26 (7) (1987) 1348–1356.
[10] Z. Chen, A. Taflove, V. Backman, Photonic nanojet enhancement of backscattering of light by nanoparticles: a potential novel visible-light ultramicroscopy technique, Opt. Express 12 (7) (2004) 1214–1220.
[11] X. Li, Z. Chen, A. Taflove, V. Backman, Optical analysis of nanoparticles via enhanced backscattering facilitated by 3-D photonic nanojets, Opt. Express 13 (2) (2005) 526–533.
[12] G. Kozyreff, N. Acharyya, Dispersion relations and bending losses of cylindrical and spherical shells, slabs, and slot waveguides, Opt. Express 24 (25) (2016) 28204–28220.
[13] T. Fatima, M.A. Fiaz, M. Faryad, On the planewave scattering from a circular cylinder with core or coating made of ENZ and DNZ mediums, J. Phys. Commun. 2 (11) (2018) 115025.
[14] T. Khudiyev, E. Huseyinoglu, M. Bayindir, Non-resonant mie scattering: Emergent optical properties of core–shell polymer nanowires, Sci. Rep. 4 (1) (2014) 1–10.
[15] C.Y. Liu, T.P. Yen, O.V. Minin, I.V. Minin, Engineering photonic nanojet by a graded-index micro-cuboid, Physica E 98 (2018) 105–110.
[16] H. Xing, W. Zhou, Y.H. Wu, Side-lobes-controlled photonic nanojet with a horizontal graded-index microcylinder, Opt. Lett. 43 (17) (2018) 4292–4295.
[17] Y. Xing, F. Shu, H. Xing, Y.H. Wu, Dynamically tunable ultralong photonic nanojets by a curved surface truncated dielectric microcylinder, Japan. J. Appl. Phys. 61 (2) (2022) 022002.
[18] T. Pahl, L. Hüser, S. Hagemeier, P. Lehmann, FEM-based modeling of microsphere-enhanced interferometry, Light: Adv. Manuf. 3 (2022) 1–13.
[19] A. Darafsheh, V. Abbasian, Dielectric microspheres enhance microscopy resolution mainly due to increasing the effective numerical aperture, Light: Sci. Appl. 12 (1) (2023) 22.
[20] I.V. Minin, O.V. Minin, Y. Cao, B. Yan, Z. Wang, B. Luk'yanchuk, Photonic lenses with whispering gallery waves at janus particles, Opto-Electron. Sci. 1 (2) (2022) 210008-1.
[21] O.V. Minin, S. Zhou, C.Y. Liu, J.A.N. Kong, I.V. Minin, Magnetic concentric hot-circle generation at optical frequencies in all-dielectric mesoscale janus particles, Nanomaterials 12 (19) (2022) 3428.
[22] V. Minin Oleg, Igor V. Minin, Optical phenomena in mesoscale dielectric particles, Photonics 8 (12) (2021) 591.
[23] M. Chirumamilla, A. Chirumamilla, A.S. Roberts, R.P. Zaccaria, F. De Angelis, P. Kjær Kristensen, R. Krahne, S. Bozhevolnyi, K. Pedersen, A. Toma, Hot-spot engineering in 3D multi-branched nanostructures: Ultrasensitive substrates for surface-enhanced Raman spectroscopy, Adv. Opt. Mater. 5 (4) (2017) 1600836.
[24] G.M. Das, R. Laha, V.R. Dantham, Photonic nanojet-mediated SERS technique for enhancing the Raman scattering of a few molecules, J. Raman Spectrosc. 47 (8) (2016) 895–900.
[25] T.W. Chang, X. Wang, A. Mahigir, G. Veronis, G.L. Liu, M.R. Gartia, Marangoni convection assisted single molecule detection with nanojet surface enhanced Raman spectroscopy, ACS Sens. 2 (8) (2017) 1133–1138.
[26] Z. Wang, B. Luk'yanchuk, L. Yue, B. Yan, J. Monks, R. Dhama, V. Minin Oleg, Igor V. Minin, S. Huang, A.A. Fedyanin, High order Fano resonances and giant magnetic fields in dielectric microspheres, Sci. Rep. 9 (1) (2019) 20293.
[27] I.V. Minin, O.V. Minin, S. Zhou, High-order Fano resonance in a low-index dielectric mesosphere, JETP Lett. 116 (3) (2022).
[28] I.V. Minin, O.V. Minin, Mesotronics: Some new, unusual optical effects, Photonics 9 (10) (2022) 762.
[29] L. Yue, Z. Wang, B. Yan, J.N. Monks, Y. Joya, R. Dhama, O.V. Minin, I.V. Minin, Super-enhancement focusing of teflon spheres, Ann. Phys. 532 (10) (2020) 2000373.
[30] A. Devilez, B. Stout, E. Bonod. N. Popov, Spectral analysis of three-dimensional photonic jets, Opt. Express 16 (18) (2008) 14200–14212.
[31] G. Gu, J. Song, H. Liang, M. Zhao, Y. Chen, J. Qu, Overstepping the upper refractive index limit to form ultra-narrow photonic nanojets, Sci. Rep. 7 (1) (2017) 1–8.
[32] S. Zhou, T. Zhou, An ultra-narrow photonic nanojet generated from a high refractive-index micro-flat-ended cylinder, Appl. Phys. Express 13 (4) (2020) 042010.
[33] A.V. Maslov, V.N. Astratov, Optical nanoscopy with contact mie-particles: Resolution analysis, Appl. Phys. Lett. 110 (26) (2017) 261107.
[34] D.E. Aspnes, S.M. Kelso, R.A. Logan, R. Bhat, Optical properties of $Al_xGa_{1-x}As$, J. Appl. Phys. 60 (2) (1986) 754–767.
[35] Y. Shen, L.V. Wang, J.T. Shen, Ultralong photonic nanojet formed by a two-layer dielectric microsphere, Opt. Lett. 39 (14) (2014) 4120–4123.
[36] G. Gu, J. Song, H. Liang, M. Zhao, Y. Chen, J. Qu, Overstepping the upper refractive index limit to form ultra-narrow photonic nanojets, Sci. Rep. 7 (1) (2017) 1–8.
[37] Y.E. Geints, A.A. Zemlyanov, E.K. Panina, Photonic jets from resonantly excited transparent dielectric microspheres, J. Opt. Soc. Amer. B 29 (4) (2012) 758–762.
[38] I.V. Minin, O.V. Minin, Diffractive Optics and Nanophotonics, Resolution below the Diffraction Limit, Springer, Cham, 2016.
[39] F. Poco John, Lawrence W. Hrubesh, Method of producing optical quality glass having a selected refractive index, 2000, U.S. Patent No. 6, 158, 244.
[40] S. Maruo, J.T. Fourkas, Recent progress in multiphoton microfabrication, Laser Photonics Rev. 2 (1–2) (2008) 100–111.
[41] X. Li, Y. Cao, N. Tian, L. Fu, M. Gu, Multifocal optical nanoscopy for big data recording at 30 TB capacity and gigabits/second data rate, Optica 2 (6) (2015) 567–570.